

VARIOUS DIFFRACTION EFFECTS AND THEIR IMPORTANCE FOR DETECTION OF INHOMOGENEITIES IN HUMAN TISSUES*

Nikola Petrović, Per Olov Risman

Mälardalen University (MDH), Academy of Innovation, Design and Engineering,
Västerås, Sweden

Abstract. *Hitherto described microwave modalities for detection of internal inhomogeneities in human tissues such as breasts and heads are by image reconstruction, requiring time-consuming computational resources. The method developed at MDH is instead based on the use of a magnetic field transducer, creating an essentially circular electrical field. This is in turn diffracted by the dielectric inhomogeneity and that signal is received by an E-field sensor in an appropriate position. The transmitting applicator is unique by no need to contact the object under study (OUS) and does not generate any surface waves at it. The primary field has properties behaving as coming from a magnetic monopole. The receiving 3D contacting applicator contains a high-permittivity ceramic and is resonant in order to provide the desired field polarisation sensitivity. The desired system properties are achieved by optimized use of the orthogonality properties of the primary magnetic, induced electric, and diffracted electric fields.*

Key words: *Diffraction, magnetic field, applicator, internal inhomogeneity.*

1. INTRODUCTION

Detection of internal inhomogeneities by microwave techniques has been an area of research for several decades [2-4]. The breakthrough was with human breasts submerged in a so-called bolus liquid in the mid 1990's [5]. Microwave imaging was then – as now – the goal, i.e. to provide images of the variations of the microwave permittivity of the various tissues and inhomogeneities in the object under study – OUS.

The choice of operating frequency is an important consideration. There are two primary factors: a) the need for dielectric contrast and b) the need for sufficient spatial resolution. Both are dealt with in sections 3.1. and 6.2 in this paper. In general, microwaves at frequencies between 0.8 GHz and 3 GHz are optimal, depending on:

Received January 1, 2020; received in revised form May 1, 2020

Corresponding author: Per Olov Risman

Mälardalen University (MDH), Academy of Innovation, Design and Engineering, Box 883, SE-72123, Västerås, Sweden

E-mail: per.olv.risman@mdh.se

*An earlier version of this paper was presented at the 14th International Conference on Applied Electromagnetics (IIEC 2015), August 26 – August 28, 2019, in Niš, Serbia [1].

1. The size of the inhomogeneity to be discovered – a lower frequency will of course result in a poorer spatial resolution.
2. A lower frequency will result in a smaller attenuation.
3. The microwave propagation path causing power losses in the tissues between the surface of the OUS where the transmitting structure is located, via the internal inhomogeneity to be discovered, and the path to the receiving structure – often described by the power penetration depth (at which $1/e$ of the power flux intensity of a plane wave remains). Another common expression for this factor is attenuation budget, which also includes the power losses of the propagation through a bolus.

A first example: Typically, the blood of a haemorrhage has 30 % higher real permittivity as well as loss factor at the typical 1 GHz frequency of operation; haemorrhages typically have volumes exceeding 20 mL – see image II in Fig. 8 – so detection is feasible if the haemorrhage is not in a deep position. The surrounding brain-matter has rather high permittivities and that of blood is still higher, and the head dimensions are comparatively large, so this low frequency is optimal. However and importantly, the head cannot be submerged in a bolus tank, as can e.g. the female breast.

A second example: Much of the female breast consists of fat tissue, which has up to ten times lower complex permittivity than brain tissue. This results in a larger penetration depth and a good dielectric contrast to tumorous tissue. However, tumours are small, which requires a higher microwave frequency for being detected. 2.5 GHz may then be a good choice.

A third example: This relates to the propagation path. If the OUS is in a bolus tank, multiple small antennas are used and each create a non-directive propagation which causes diffraction phenomena over most of the OUS. Signals are then received by several antennas, excluding the nearest to the transmitting one (too strong direct signal, burying the diffraction signals) and also the opposite ones (too high attenuation budget, i.e. the system becomes more expensive and prone to external interferences). – With our system principle – see Fig. 5 – the induced electric field “directivity” has a conical shape with no field at the axis. This reduces the diffracted fields emanating from the opposite side to the receiving structure location, and diffraction from inhomogeneities up to about 90° sideways are promoted and measured on the OUS surface.

Another factor: It is concluded from the above that transmission/detection across, and preferably about or slightly more than 90° sideways is needed with microwave systems. Signals emanating from the central regions of the torso are not measurable in practice. Protruding body-parts such as the head (albeit with reservations), female breasts, legs, and arms are feasible. The OUS surface waves have been and are still “neutralised” by this immersion of the OUS in a mixture of liquids (typically water-glycerol) having a microwave permittivity similar to that of the OUS. That method is, however, not possible with heads.

The submersion of the OUS in a liquid tank with similar permittivity properties to the tissues provides a simple solution to several antenna design issues. Since these are submerged in the bolus liquid and at a distance from both the tank walls and the OUS, the nearfields are in the homogeneous liquid. Simple propagating fields can then be assumed at the OUS, and reflections at the tank walls become insignificant. In addition, the large bolus volume contacting the OUS and these having similar permittivity solves a very significant problem: that of surface waves else created along the surface of the object under OUS. However, submerging a human head in a bolus is practically impossible, so other means of eliminating of the surface waves become necessary. The hitherto most successful efforts are by the EM-Tensor company in Austria [6, 7], using a thin bolus layer between the head and

a metallic hood. A large number of fixed ceramic antenna applicators in the hood is used, with a large number of sets of transmission paths. The tomographic computations are then made in two basic steps: a first to compute the OUS surface dimensions, and a second to compute the structure of the internal inhomogeneities in the OUS.

All existing systems such as that by EM-Tensor – as well as our and any future systems – employ diffraction effects. Somewhat astonishingly, only our group at MDH has not only studied and analysed the actual diffraction phenomena, but we are also using our system for direct detection of these, as opposed to using multiple antennas [2] submerged with the OUS in a large tank.

In the following, we firstly describe the diffraction phenomena in and at a lossy dielectric wedge and lossy spheres, for the latter we also discuss the polarisation and directions of the external diffracted fields which are actually much of the basis of our work on direct detection of inhomogeneities in the OUS. Our system with its main component – the special quasistatic B-field transmitting applicator – is then described. Numerical FDTD modeling of a simple phantom head is then addressed, using a new field subtraction method showing the diffracted field patterns. Finally, some experiments are described, and conclusions on the limitations of discerning haemorrhages are presented.

2. WHAT DIFFRACTION EFFECTS OF POSSIBLE INTEREST EXIST?

2.1. General

Several kinds of diffraction phenomena have been studied for many years. Some are a nuisance in e.g. microwave oven food heating, and some phenomena have only extremely complicated analytical solutions. The physical “explanation” to some phenomena is actually not possible by analytical calculations, so the geometric theory of diffraction may be a way out. This is based on Huygen’s principle but requires experimental determination of a so-called canonical constant. Of interest in our context is, however, that some diffraction effects cause field polarisations that are very useful for detection of internal inhomogeneities.

2.2. The edge overheating and centre focussing effects

The edge overheating effect (in e.g. microwave oven food loads) is a significant issue and is polarisation dependent. It is illustrated in Fig. 1 a) and b), obtained with numerical modeling using the Quickwave FDTD software [8]. They show the power distributions in a 90° dielectric wedge illuminated from below by a 2,45 GHz TEM-wave. The impinging E-field in Fig. 1 a) is in the direction of the wedge tip (in-out in the paper); it is left-right in Fig. 1b). The strong heating in the wedge regions is up to four times stronger to what would occur with vectorial addition of fields coming from both directions to the surfaces.

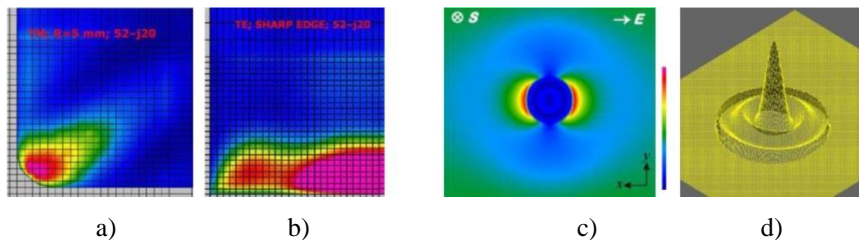


Fig. 1 Illustrations of some diffraction phenomena

The strength of the phenomenon can be deduced by a first order theory based on the geometric theory of diffraction, which has also been confirmed by numerical modeling and experiments [9]. It turns out that the statements in many textbooks that the effect results from simple addition of wave energy irradiating the edge from two directions (from the side and from above, instead of one direction) is in error. As an example for $\varepsilon = 52-j20$ and wedge angle 90° , the maximum power density in the tip is typically 4 times higher than some distance away from the tip, and 6 times higher for wedge angle 60° , for a single plane wave irradiation. For ε' about 15 the factor is about 2 for wedge angles between 30° and 60° . The effect has almost disappeared for ε' about 4. The size of the overheated zone also varies with ε' ; the length becomes 12 mm for a 60° wedge. The first order equation for the electric field maximum E_e inside the edge tip is:

$$\frac{E_e}{E^i} \approx \frac{2}{1+\sqrt{\varepsilon}} + \frac{0.50 \cdot (90-\alpha)}{90+0.50 \cdot \arcsin(1/\sqrt{|\varepsilon|})} \quad (1)$$

where E^i is the incident field and the wedge angle is 2α , with all angles in degrees. The first term is a wave potential term which also gives the field just inside a large flat load, and the second term a diffraction source term. The factor 0.50 is a so-called canonical constant that cannot be derived theoretically and was determined by numerical modeling [9].

It should be noted that the direction of incidence has a very small and only second order influence on the effect, as long as it is within the 'free' ($180-2\alpha$) angle. Impinging waves which do not hit the edge tip first will also create surface waves. The wave potential term will then change, and with that the edge overheating effect.

Fig. 1 c) and d) show the phenomenon of a remarkable "focussing" effect of power density to the centre region of a round object having a circumference of about one free space wavelength. Fig. 1c) is an illustration by FDTD modeling with the Quickwave software [8] of the momentary overall average E field in and at a 40 mm diameter sphere with $\varepsilon = 40-j16$ illuminated by a 2,45 GHz plane wave with its E field with relative amplitude 10 (green). Magenta = maximum = +23 units, dark blue = 0. The pattern is an E-field-dominated hybrid mode of the second kind: EH_{202} (the TE and TM type modes are non-separably coupled). The external mode is TM_{y01} with the same spherical mode designation (by the Bromwich method [10]) and has similarities with the lowest circularly cylindrical TM_{z00} resonant mode bound to a long thin z-directed dielectric exposed to an E field parallel to the axis. Fig. 1d) shows the power density pattern as the same load as in Fig. 1c), in the same plane. The radius of the volume in which the power is larger than half the maximal is about 3,2 mm, corresponding to about 4 % of the overall volume. The average power density in most of the load volume is about 7 % of that at the centre.

Fig. 2 left shows the standard radar cross section analytical solution for a metal sphere. It is seen that the main external surface resonance effect shown in Fig. 1c) and d) is confirmed by the first maximum. Fig. 2 right shows the relative absorbed power flux density ($1/r^2$, y axis) in free spheres under plane wave irradiation, as function of the radii in mm (x axis) and with the complex permittivity $\varepsilon = \varepsilon' - j\varepsilon''$ as parameter, at 2,45 GHz, by analytical calculations. Note the maxima at 20 mm radius for both $\varepsilon = 16-j8$ and $52-j20$. There are also weaker maxima at 40 mm radius.

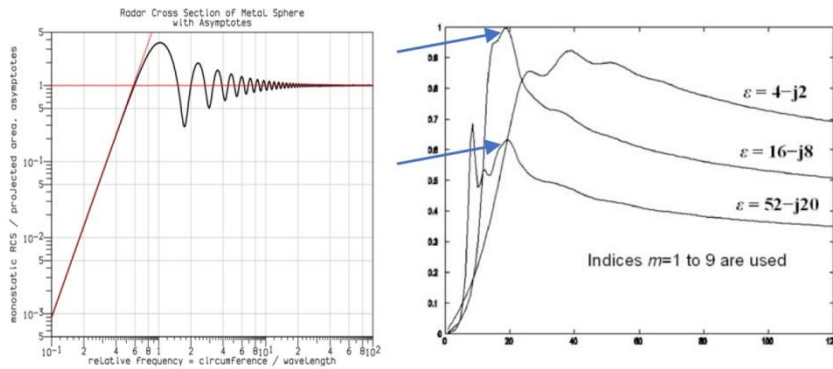


Fig. 2 Illustrations of Mie scattering of spherical objects in free space

The phenomena shown in Figs 1 and 2 are manifested for example by a chicken egg in its basic shape, raw or boiled, deshelled or not, shattering violently in any microwave oven within about half a minute. This is thus not by any quasi-optical focussing effect, but instead by the formation of an external surface wave resonance, basically being maximal for the object circumference being about one free space wavelength [11].

Of course, related phenomena occur also for cylindrical objects. It is to be noted that it is possible to employ the radar cross section differences for discerning of free objects of different sizes by operating a multiantenna detection system, using also the polarisation of the diffracted waves, then in the region circumference/wavelength from about 0.6 to 1.8.

3. DIFFRACTION PHENOMENA VS ROUNDED OBJECT SIZE AND PERMITTIVITY

3.1. Absorbed and diffracted power

A good beginning is to study the analytically solvable scenario of a dielectric lossy sphere under plane wave irradiation. Fig. 3 a) shows the case of spheres at 2,45 GHz (the ISM band for e.g. microwave ovens), with the radius as variable and complex permittivity as parameter. One can see the TE_{101} resonance at about 8 mm radius (upper arrow), the TM_{101} at 12 mm, and the particular overall EH_{202} and external TM_{y01} resonant at 20 mm. The first index m for TE_{mnp} modes is for H field maxima along the z axis ($\theta = 90^\circ$), n is for H field variations along the equator and p for the E field in the radial direction. Importantly, the resonant TE_{101} mode exists down to very small diameters, down to where the constant quasistatic field takes over. The mode is that of a magnetic dipole, as shown by the H field lines in the right Fig. 3 b) [12] at free resonance for $\epsilon = 14$. The TM_{101} mode is that of an electric dipole and its E-field lines are shown in Fig. 3 b) left at free resonance for $\epsilon = 14$.

Fig. 3 c) shows the analytically calculated absorbed (red) and diffracted (blue) relative power at 2,45 GHz under plane wave irradiation of spheres with $\epsilon = 52 - j20$, with the radius as variable. Fig. 3 d) shows the diffracted power flux density into a lossless medium with $\epsilon = 40$, from a spherical object with $\epsilon = 70 - j10$, with its radius as variable, at 2,45 GHz. The red curve is for the TE_{101} and TM_{101} fields only, and the magenta curve for all modes up to index 5, i.e. TE_{m05} and TM_{m05} . It is seen that the $m = 1$ term dominates up to 20 mm radius, and that the diffraction is very weak up to about 5 mm radius, after which it raises linearly with the radius.

This is consistent with Rayleigh's law: the same small object diffraction proportional to λ_0^{-4} , but it can be shown that the reduction is approximately by r^{-6} at constant frequency in the steepest part of the curve. However, a comparison with the absorbed power flux density shows that the diffracted power flux is twice or more stronger than the absorbed.

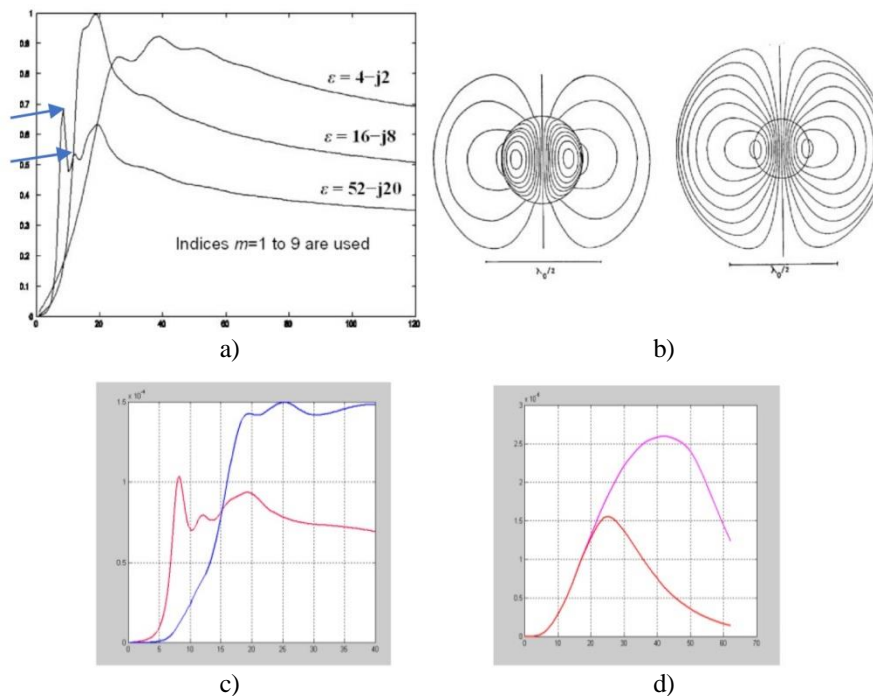


Fig. 3 Diffraction phenomena at smaller objects

To sum up:

1. A high quotient between the ϵ' values give better diffraction;
2. a significant quotient between only ϵ'' gives a weak diffraction;
3. the diffracting object needs to be at least 10 mm in diameter at 2,45 GHz for providing a "good" diffraction in a typical human object such as a head or breast containing some inhomogeneities. The sensitivity increases significantly with a fully homogeneous OUS model – see the section on investigations of a test scenario.

3.2. Diffracted field patterns

Fig. 4 shows the numerically modelled maximal momentary E_y field (left) and H_x field (right) for a 16 mm diameter sphere with $\epsilon = 40-j16$ in free space, at 2,45 GHz. The irradiation is by E_z and H_y , so the fields shown in the images are both perpendicular to those of the irradiating wave. The scaling is equalised (i.e. with a normalisation providing equal electric and magnetic field energies) in the zy plane shown in the figure.

It is seen that there is a sideways propagation, i.e. perpendicularly to that of the impinging wave. By studies of these and other fields and their variations along the axes

one can deduce that the mode is TE_{101} ; see Fig. 3 b) right. It is characterised by diffracted fields in mainly the zy plane.

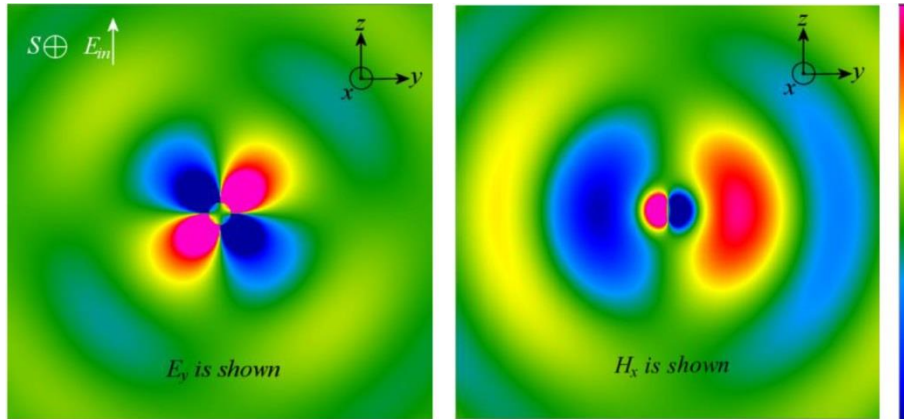


Fig. 4 Momentary fields at a 16 mm diameter sphere at 2,45 GHz

4. OUR SYSTEM – OVERVIEW AND FUNCTION

4.1. General

Our most recent system at MDH [13, 14] is not based on a need for complex and time-consuming mathematical algorithms and complicated microwave circuitry. We instead directly employ certain internal diffraction phenomena, using a movable set consisting of a special transmission applicator surrounded by receiving devices, see the outline in Fig. 5. The transmission applicator has the unique property of acting as a “magnetic monopole” with the electric field being created within the OUS and no such components on its surface. An outline of the fields generated by the transmitting applicator and the diffracting object is shown in Fig. 5. The H field (blue lines) induces a “circular” E field (in-out in the illustration; red circles), both hitting the diffracting “inhomogeneity object” (green) essentially as a TEM wave. Mainly the “ends” or periphery of this produce fields as shown in the figure with the resulting E fields shown as red arrows. This, plus the diffracted field directions as shown in Fig. 4, result in a minimum diffraction field straight outward from the central projection of a larger inhomogeneity object than that shown in Fig. 5, but then instead diffracted fields from the edges of the object.

With the geometry of the scenario there will thus be an E field component perpendicular to the direction of the primary E field, i.e. radially as seen from the OUS surface. This is important, since both the stronger primary field

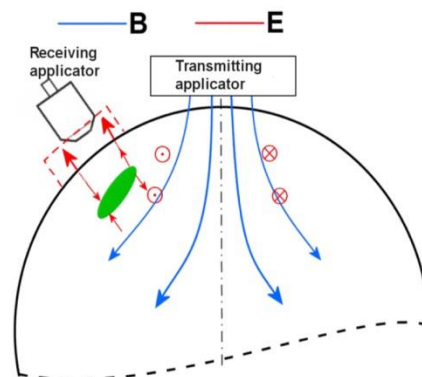


Fig. 5 System overview

and any other surface-parallel E field are enhanced (i.e. reflected back into the OUS) by the magnetic wall effect. However, in the case of the non-contacting receiving applicator, the surface-perpendicular field will be stronger in the airspace just outside the OUS, by the D field vector continuity.

The procedures for collecting and using the data are tentatively as follows. – With a fixed position of the transmitting device, the receiving device (or two diametric such devices) is moved around the skull surface, in a circumferential region around the axis of the transmitting device and at an azimuthal angle between about 30 and 70° (see Fig. 5), which will be the best for receiving the diffracted signals. These are then recorded with the geometric positions of the devices, in for example 30 locations of the receiving device. The mechanical set of devices is then moved to another location, and the same procedure is carried out, in e.g. four locations of the transmitting device. The memorised geometric and signal data are then treated in a relatively simple software, providing an almost immediate “map” of the signal strengths over the skull surface region. This will provide a correlation between the (continuous) haemorrhage periphery as “seen” from the outside. More advanced algorithms may also be developed, for providing haemorrhage depth indications. – Of course, the same principles are applicable also for breasts and other protruding body parts.

4.2. The transmitting applicator

This is shown in Fig. 6 left. There are a pair of current feeds in each gap in the inner ring; these are coupled for creation of a circulating current in it, at about 1 GHz with an overall applicator diameter of about 80 mm as in the picture. The double gaps are for optimising the purity of the created H field, as are the outer rings. Fig. 6 mid shows the numerically modelled axial H field amplitude in the axial plane, in dB scale, with a 6 mm thick OUS outer layer with $\epsilon' = 20$ and $\sigma = 0,4$ S/m at 2 mm distance, and an inner continuum with $\epsilon' = 45$; $\sigma = 0,8$ S/m – i.e. simulating a human head. There is thus a certain attenuation, but it is seen that the applicator largely functions as a magnetic monopole.

The particular properties of the quasistatic field emanating from the applicator results in virtually no surface waves at all being created in the OUS surface region. This allows the device to be located some millimetres away from the OUS – no bolus liquid is needed and the applicator can easily be moved over the OUS surface.

The diameter 80 mm at 1 GHz is of course a disadvantage, but only one device is needed and the resulting propagating waves in the OUS are favourable: basically radially outwards from the device axis. The optimum positions of the receiving devices is not close to the transmitting device sideways at the OUS, as shown in Fig. 5. The disadvantage that there will be no or a very weak induced E field at the transmitter axis is of course compensated in practise by moving the whole set, as addressed earlier.

4.3. The receiving device

This is still under development, and a working design is shown in Fig. 6 right. It is resonant at about 1 GHz. The overall diameter of the high permittivity ceramic (magenta in the Fig.; $\epsilon' = 73$) is 20 mm. The applicator mode is of the circular TM_{01} type, resulting in an axial E field at the sensing end. The frustum conical part provides a nulling of the reception properties of any radial (up-down in the Figure) E field components. This

results in a filter function for sensing mainly the radially outwards-going diffracted E field at the OUS surface.

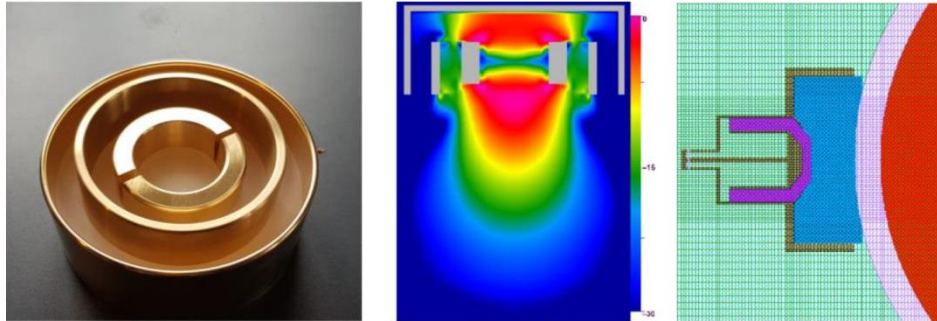


Fig. 6 The transmitting applicator (left), its axially directed B field (mid), and the receiving applicator.

These properties of the receiving device are quite desirable, but expensive to manufacture, in particular since at least two are needed in a complete practical set-up. There are also issues with disturbances by the connected cables as seen by the curve fluctuation in Fig. 8 III and 8 IV, so a design with a built-in amplifier, AD converter, a small battery and Bluetooth transmitter is now under consideration. It is then to be noted that only the signal amplitude and not phase are needed, and that the activation needs to be only about 1 % of the total time for an overall measurement session.

It is to be noted that the bolus layer is also under development and can be very thin, but there is a need for contacting to the OUS, so a thin flexible rubber film may be used. A particular issue is then also the microwave properties of the contacting skin layer, which is currently under investigation by particular *in vivo* measurements. Without contacting, there will be a sensitivity to any residual surface waves, which have an axial E field component. The resonance properties do virtually eliminate the influences by extraneous propagating fields in the surroundings, and by that simplifies the electronics. A particular advantage with the principle is that no phase measurements are needed. This virtually eliminates calibration procedures, which are typically both complicated and time consuming with systems such as in [6, 15]. Components and connections become much less expensive.

5. INVESTIGATION OF A TEST SCENARIO AND EXPERIMENTAL WORK

5.1. The test scenario and numerical modeling

Fig. 7 A and B show the head model with a 20 cm³ cylindrical water inhomogeneity, as seen in the images. Frequency 1 GHz, about 12 million voxels, 0.13 mm smallest distance between z planes, main voxel setting with 0.6 mm sides.

Fig. 7 A and B illustrate the modeling scenario with the transmitting applicator on top of the simulated head and an asymmetrically located water object (magenta) with diameter 25 mm and height 40 mm. The head maximum diameter is 220 mm and there is a 6 mm thick bone and skull layer (brown) outside the simulated homogeneous brain, being by a ternary liquid mixture in the experiments. A numerical modeling result is

shown in Fig. 7 C and D, with the use of a new Quickwave [8] subtraction module allowing field images (subtracted average/ amplitude or momentary at the same timestep), in this case with and without the water object. Fig. 7 C shows the difference in the axially directed E field amplitude in a vertical plane 10 mm in front of the central plane, in linear scale, i.e. magenta = positive max; green = 0, darkest blue = negative max. Fig. 7 D shows the same but now in the central plane and with the span between darkest blue and magenta being 40 dB. Fig. 7 E is the difference in the left-right-directed E field amplitude in a vertical plane near the centre of the object in Fig. 7 A and B, between scenarios with and without the water object (linear scaling). Fig. 7 F has the same scaling as Fig. 7 E, but now in a horizontal plane through the centre of the water object.

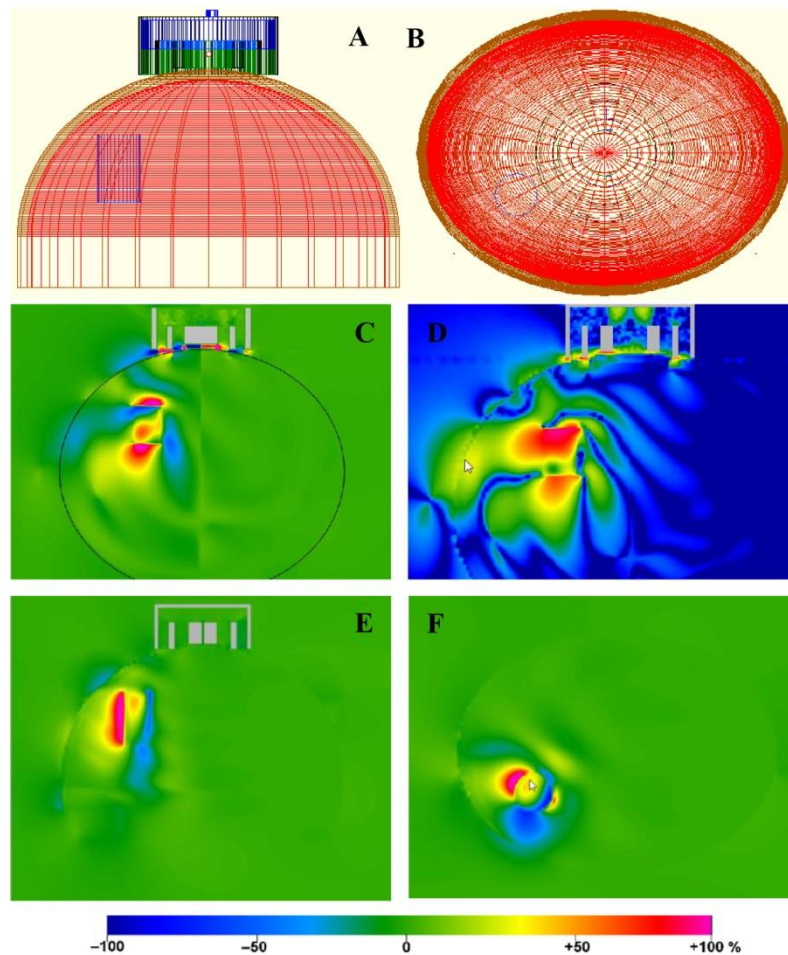


Fig. 7 The test scenario and numerical analysis

Fig. 7 C and D show that the field is stronger to the left of the water object and weaker on the other side. It is to be noted that the scenario is a replication of an actual experimental

set-up – see Fig. 8 A. The signal difference as “measured” as the numerical result in the position shown by the arrow in Fig. 7 D was +4 dB with/without the water object present.

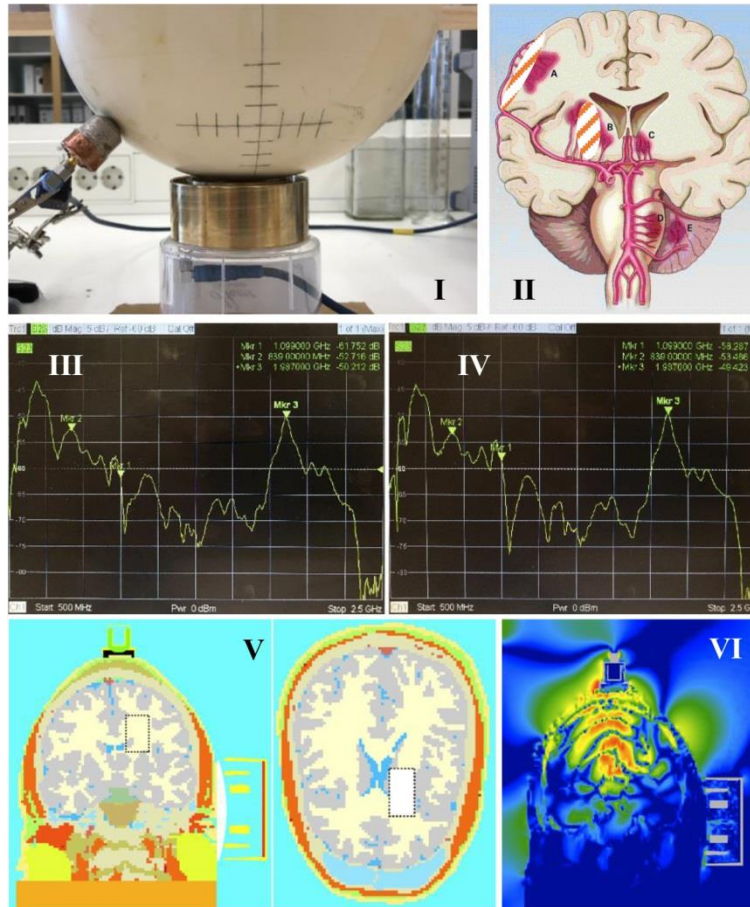


Fig. 8 Experimental setups and results; skull/brain investigation

It is seen that the subtracted field is stronger above and below the water object, and weaker straight outwards. The images confirm the theory on the main diffracted fields emanating from the “ends” of the enclosed object.

The results in this section clearly shows the usefulness of our field subtraction facility. Even if its usability is excellent for our diffraction studies described here, it can have many other uses, such as qualitative and quantitative detection of faults or deviation sensitivities in various objects and systems such as microwave filters and similar components.

With this system with somewhat larger inhomogeneities we have by FDTD modeling obtained a difference of up to +15 dB in a homogeneous material simulating brain permittivity, at a level of about 50 dB signal overall attenuation.

5.2. Experimental work

Fig. 8 I is a picture of the experimental set-up with the experimental skull. It was specially made and contains strontium titanate for increasing the permittivity: $\epsilon' \approx 15$ and $\sigma \approx 0.3$ [16]. The transmitting applicator is placed under it and the receiving applicator at the side. A thin-wall glass vial with water in gelled form was submerged in the water and glycerol mixture with properties simulating the average permittivity of white and grey matter [17] and moved around for obtaining the best signal change. This was about 3.5 dB and corresponds rather well to the position shown in Figs 7 A and B. The signal differences are shown in Fig. 8 III and IV and confirm our modeling results. They show the measured S_{21} without (III) and with (IV) the water clot. The sensing frequency of the receiving applicator is marked as Mkr 1. The difference with/without the clot is about 3.5 dB.

It is of importance that there are virtually no surface waves. This applies to both the modeling and the experiments. However, the transmitting applicator did not have a good balun feeding, since it represents an extremely low impedance. Furthermore, the receiving applicator design has imperfections. These issues and extraneous interferences are the reasons for the irregularities in the S_{21} curves.

6. DISCUSSION AND CONCLUSIONS

6.1. General on haemorrhage detection in human heads

Fig. 8 II shows a cross section of a human brain with marked regions of typical haemorrhages. The most interesting and possible to detect with microwaves are marked A and B in the image – the others are too deep-lying and detection will also be hindered by the major normal inhomogeneities in this central region, as seen in the image.

The quite large natural inhomogeneities in the head are characterised by such different dielectric composition that they will inevitably cause diffraction effects. The question is then to what extent these inherent diffraction fields may overshadow those by a haemorrhage. It seems likely that the volume of the haemorrhage must be comparable or larger than those of the surrounding natural inhomogeneities of the brain, for sufficiently reliable haemorrhage detection to be achievable by direct detection methods such as ours. Reliable microwave detection of deep haemorrhages is in our opinion possible only with acquisition of S_{mn} phase and amplitude data using more than a hundred multi-switched antennas and advanced and time-consuming computations. True 3D tomographic images are then obtainable, but even then the so-called attenuation budget will become problematic and require almost extreme dynamic ranges of the amplifiers, etc.

6.2. Studies of the Austin man head

All kinds of inhomogeneities in the skull will cause diffraction phenomena, as well as reflection and absorption. In order to quantify this, the head of the Austin man [18] was converted for use in the modeling software, with 2 mm cubical voxels and the specified dielectric data of the 30 kinds of substances, at 1 GHz. The model is shown in Fig. 8 V, with a blood clot having dimensions 18 mm \times 34 mm and height 30 mm (i.e. a volume of about 18 cm³). This was asymmetrically located.

A result of the subtraction of averages with/without the blood clot, of the x-directed E field in the y plane giving the strongest diffraction phenomena, is shown in Fig. 8 VI, in

decibel scaling. The signal to the receiving applicator was not evaluated but it is seen that the strongest signal is just to the right of it. The difference is 3 dB.

An important conclusion is that the disturbing wave phenomena caused by the many inhomogeneities and widely different complex permittivities: ϵ' from 1 (air-pockets) to 70 and up to $\sigma = 2.5$ S/m for the cerebrospinal fluid – will require quite voluminous inhomogeneities or these to be located close to the skullbone. It seems that deep-lying inhomogeneities (e.g. B in Fig 8 II) need to be larger than about 30 cm^3 at 1 GHz, and that flat or spread-out inhomogeneities need to have surface areas of at least 25 cm^2 for non-tomographic multi-antenna systems to be useful. Our investigations on this are continuing.

6.3. Conclusion

As described in this presentation our system has some unique properties. The key elements and their function are related to the polarisation and field orthogonality phenomena with a magnetic field emitting device creating a “rotating” electric field in the OUS. The internal inhomogeneity then creates orthogonal diffracted fields. The combination of a special transmitting device and a resonant receiving device requires only amplitude measurements, which significantly reduces system complexity, cost and some calibration issues, while achieving good sensitivity. We therefore expect our overall system approach to become a viable and cost-effective class of equipment for detection of human body-part abnormalities.

Our method of direct measurements of diffraction effects by internal inhomogeneities such as haemorrhages and tumorous tissue provides about the same operational procedure as does X-ray mammography and partially also ultrasound, but at a projected much lower cost. A further contributing factor to the low cost is that complicated computations are not needed, which also saves time since our method provides immediate results. The contrast is by permittivity differences which are principally not correlated to X-ray grayscale representation. A combination of the two methods will thus provide much reduced false positive/negative medical conclusions.

Acknowledgement: *Our work is financially supported by the Swedish Knowledge Foundation (KKS) through the project Embedded sensor systems for health plus (ESS-H+), project number 20180158.*

REFERENCES

- [1] P.O. Risman and N. Petrovic, “Detection of Diffraction Effects by Brain Haemorrhages with a Special Microwave Transmission System”, In Proceedings of the 14th International Conference on Applied Electromagnetics (IIEC 2019), Aug 2019.
- [2] P.M. Meaney, M.W. Fanning, Dun Li, S.P. Poplack, and K.D. Paulsen, “A clinical prototype for active microwave imaging of the breast”, *IEEE Transactions on Microwave Theory and Techniques*, vol. 48, no. 11, pp. 1841–1853, Nov 2000.
- [3] S. Y. Semenov et al., “Microwave tomography: two-dimensional system for biological imaging”, *IEEE Transactions on Biomedical Engineering*, vol. 43, no. 9, pp. 869–877, Sept. 1996.
- [4] A. Franchois, A. Joisel, C. Pichot and J. C. Bolomey, “Quantitative microwave imaging with a 2.45-GHz planar microwave camera”, *IEEE Transactions on Medical Imaging*, vol. 17, no. 4, pp. 550–561, Aug. 1998.
- [5] P.M. Meaney, K.D. Paulsen, A. Hartov and R.K. Crane, “An active microwave imaging system for reconstruction of 2-d electrical property distributions”, *IEEE Transactions on Biomedical Engineering*, vol. 42, no. 10, pp. 1017–1026, Oct. 1995.
- [6] I. El Kanfoud, V. Dolean, C. Migliaccio, J. Lanteri, I. Aliferis, C. Pichot, P. Tournier, F. Nataf, F. Hecht, S. Semenov, M. Bonazzoli, F. Rapetti, R. Pasquetti, M. de Buhan, M. Kray and M. Darbas, “Whole-

- microwave system modeling for brain imaging”, In Proceedings of the 2015 IEEE Conference on Antenna Measurements Applications (CAMA), pp. 1–4, November 2015.
- [7] P. Tournier, M. Bonazzoli, V. Dolean, F. Rapetti, F. Hecht, F. Nataf, I. Aliferis, I. El Kanfoud, C. Migliaccio, M. de Buhan, M. Darbas, S. Semenov and C. Pichot, “Numerical modeling and high speed parallel computing: New perspectives on tomographic microwave imaging for brain stroke detection and monitoring”, *IEEE Antennas and Propagation Magazine*, vol. 59, no. 5, pp. 98–110, October 2017.
- [8] QWED Company, QuickWave 3D – Complete 3D electromagnetic simulation, 2019 (accessed December 2019).
- [9] P.O. Risman, “Diffraction phenomena inside dielectric wedges – qualitative theory and verification by modelling and experiment”, In Proceedings of the MIKON 2008 conference paper A7/1, Wroclaw, Poland.
- [10] S. Gallagher and W.J. Gallagher, “The spherical resonator”, *IEEE Trans. on Nuclear Science*, vol. NS-32, no. 5, pp. 2980–82, October 1985.
- [11] P.O. Risman and M. Celuch-Marcysiak, “Electromagnetic modelling for microwave heating applications”, invited paper, In Proceedings of the 13th Intl.Conf. on Microwaves, Radar and Wireless Communications, Wroclaw, May 2000, vol. 3, pp. 167–182.
- [12] M. Gastine, L. Courtois and J.L. Dormann, “Electromagnetic Resonances of Free Dielectric Spheres”, *IEEE Trans. Microwave Theory and Techniques*, vol. MTT-15, pp. 694–700, December 1967.
- [13] N. Petrovic, M. Otterskog and P. O. Risman, “Antenna applicator concepts using diffraction phenomena for direct visualization of brain hemorrhages”, In Proceedings of the 2016 IEEE Conference on Antenna Measurements & Applications (CAMA), Syracuse, NY, 2016, pp. 1-4.
- [14] N. Petrovic, M. Otterskog and P. O. Risman, “Breast tumor detection with microwave applicators in open air”, In Proceedings of the 2017 IEEE Conference on Antenna Measurements & Applications (CAMA), Tsukuba, 2017, pp. 272-274.
- [15] P. M. Meaney, K. D. Paulsen and J. T. Chang, “Near-field microwave imaging of biologically-based materials using a monopole transceiver system”, *IEEE Transactions on Microwave Theory and Techniques*, vol. 46, no. 1, pp. 31–45, Jan. 1998.
- [16] M. Otterskog, N. Petrovic and P. O. Risman, “A multi-layered head phantom for microwave investigations of brain hemorrhages”, In Proceedings of the 2016 IEEE Conference on Antenna Measurements Applications (CAMA), Oct 2016, pp. 1–3.
- [17] P. M. Meaney, C. J. Fox, S. D. Geimer and K. D. Paulsen, “Electrical characterization of glycerin: Water mixtures: Implications for use as a coupling medium in microwave tomography”, *IEEE Transactions on Microwave Theory and Techniques*, vol. 65, no. 5, pp. 1471–1478, May 2017.
- [18] J. W. Massey and A. E. Yilmaz, “Austinman and austinwoman: High-fidelity, anatomical voxel models developed from the vhp color images”, In *Proceedings of the 38th Annual International Conference of the IEEE Engineering in Medicine and Biology Society (EMBC)*, August 2016, pp. 3346–3349.